solids

MDPI

Article

Precursor-Based Syntheses of Mo(C,N,O)$_x$, Molybdenum Carbide, Nitride, and Oxide Applying a Microjet Reactor

Mana Abdirahman Mohamed [1], Oliver Janka [1], Susanne Harling [1] and Guido Kickelbick [1,2,*]

[1] Inorganic Solid-State Chemistry, Saarland University, Campus C4 1, 66123 Saarbrücken, Germany; mana.mohamed@uni-saarland.de (M.A.M.); oliver.janka@uni-saarland.de (O.J.)
[2] Saarene—Saarland Center for Energy Materials and Sustainability, 66123 Saarbrücken, Germany
* Correspondence: guido.kickelbick@uni-saarland.de

Abstract: Composite materials such as molybdenum carbides, nitrides, oxides, and mixed anionic compounds like Mo(C,N,O)$_x$ embedded in carbonaceous matrix exhibit promising potential as anode materials for lithium batteries, with a preference for fine-grained morphologies. In this study, we present a novel synthetic approach involving an inorganic–organic hybrid precursor precipitated from aqueous solutions of ammonium heptamolybdate and one of two organic species: 1,8-diaminonaphthalene (1,8-DAN) or hexamethylenediamine (HMD). The precipitation reaction can be carried out in a beaker and in a continuous process using a microjet reactor. This enables the synthesis of precursor material on the gram scale within minutes. The pyrolysis of these precursors yields mixtures of Mo(C,N,O)$_x$, MoO_2, Mo_2C, Mo_2N, and Mo, with the choice of organic compound significantly influencing the resulting phases and the excess carbon content in the pyrolyzed product. Notably, the pyrolysis process maintains the size and morphology of the micro- to nanometer-sized starting materials.

Keywords: continuous synthesis; molybdate; 1,8-diaminonapthalene; hexamethylenediamine; inorganic–organic hybrid material; pyrolysis; molybdenum oxide carbide; composite material

Citation: Abdirahman Mohamed, M.; Janka, O.; Harling, S.; Kickelbick, G. Precursor-Based Syntheses of Mo(C,N,O)$_x$, Molybdenum Carbide, Nitride, and Oxide Applying a Microjet Reactor. *Solids* **2024**, *5*, 443–459. https://doi.org/10.3390/solids5030030

Academic Editors: Andrei V. Shevelkov and Maxim N. Sokolov

Received: 8 July 2024
Revised: 15 August 2024
Accepted: 28 August 2024
Published: 4 September 2024

1. Introduction

Current lithium-ion batteries (LIBs) contain graphite as anode material, which has a relatively low capacity of 372 mA h g^{-1}. The limited capacity of intercalation materials, e.g., graphite and other types of materials, such as lithium titanate, $Li_4Ti_5O_{12}$ (LTO), can be exceeded by conversion materials, e.g., nanoparticles of transition metal oxides, e.g., Fe_2O_3, CoO, and CuO. These materials are being explored for improved battery performance [1–4].

Molybdenum oxides, showing theoretical capacities of 837 mA h g^{-1} for MoO_2 and 1117 mA h g^{-1} for MoO_3, are also potential candidates for anode materials. Molybdenum carbides like Mo_2C and MoC_x (x = 0.43–0.75) exhibit beneficial lithium storage properties relative to simple oxides because of their better chemical stability, electrical conductivity, and excellent mechanical properties [1]. The combination of the properties of molybdenum oxides and carbides has the potential to create a new class of electrode materials for LIBs [1].

Generally, the industrial production of molybdenum carbides proceeds via a powder metallurgical process, in which the molybdenum oxides are reduced to the element by applying hydrogen. Afterwards, the metal is carburized with carbon powders at very high temperatures (1500–2000 °C). This process is extremely energy intensive, and the formed Mo_2C cannot be used for application in LIBs due to the lack of the required high specific surface area. Therefore, low-temperature preparation routes are preferred for the electrochemical applications [5].

One potential method for the production of valuable materials is chemical vapor deposition (CVD), in which carbonaceous gases like CH_4, C_2H_6, and CO, along with Mo-containing precursors, are used for the deposition of the materials on various substrates.

While showing some advantages to the industrial method, still the pore structure and purity of the resulting Mo_2C are not satisfying. In addition, the equipment costs of CVD systems are quite high [5,6]. Alternative synthesis strategies include the use of molecular precursors in pyrolytic reactions at much lower temperatures than the previously mentioned techniques. More moderate reaction conditions, in addition to a diverse composition of precursors, allow a more flexible adjustment of the size and morphology of the final product, which is beneficial for the LIB application [5].

Several reports in the literature show that suitable compounds can be obtained from precipitation reactions. Subsequent pyrolytic reactions allow the preparation of the targeted compounds. In the following, several methods for the carbothermic reduction of molybdenum carbide via a precursor route are listed. Precursors as previously studied starting materials were mixtures of molybdate and 2-methylimidazole [1], aniline [7], p-phenylenediamine [8], melamine [9], and dicyandiamide [10]. A novel procedure for the synthesis of Mo_2C and Mo_2N nanoparticles was reported by Giordano et al. It was based on a process in which $MoCl_5$ was dissolved in ethanol, and urea was subsequently added to form a polymeric, glassy phase. Later, thermal treatment under nitrogen gas flow was applied, and by changing the molar ratio of metal to urea, molybdenum nitride or the respective carbide was synthesized [11]. A simple way to prepare Mo_2C nanoparticles on 3D carbon microflowers by self-polymerization of dopamine was found by Huang et al. who performed the pyrolysis under argon flow [12]. A new route for mesoporous and nanoscale Mo_2C/Mo_2N heterojunctions was designed by Li et al. using a dopamine–molybdate coordination precursor with silica nanoparticles [13]. Finally, Wang et al. found that a mixed salt precursor containing a molybdenum–hexamethylenetetramine complex could be pyrolyzed under an argon atmosphere [14].

Several phases can be obtained by such decomposition reactions, such as orthorhombic HT-Mo_4O_{11} [15,16], monoclinic MoO_2 [16], orthorhombic Mo_2C [17] (Figure 1a), and cubic Mo [18]; thus, reaction conditions have to be accurately controlled [6]. Around 873 K, MoO_2, MoC, and C exist in an equilibrium. At this point, molybdenum oxide carbide can be obtained; above 923 K, Mo_2C is the stable phase [19]. It is also possible to obtain other molybdenum carbides such as cubic (Figure 1b) or hexagonal (Figure 1c) MoC_x. Furthermore, it is also possible to obtain Mo_2N due to the use of amines in the hybrid precursors [11,19].

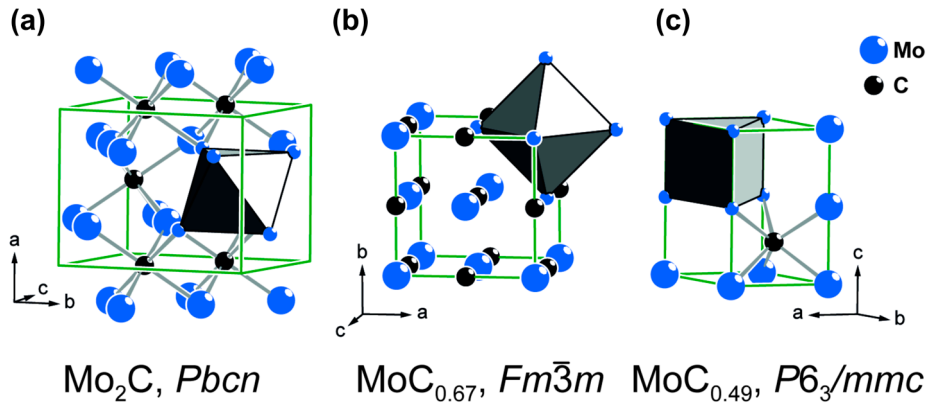

Figure 1. Crystal structures of (**a**) orthorhombic Mo_2C [17,20], (**b**) cubic $MoC_{0.67}$ [21], and (**c**) hexagonal $MoC_{0.49}$ [22]. Mo atoms are illustrated in blue, C atoms in black. The space groups are provided.

A prominent source of molybdenum in the precursors is ammonium heptamolybdate $(NH_4)_6Mo_6O_{24}$ (AHM), which often forms precipitates together with cationic organic compounds. Mo_2C can be obtained after pyrolysis of the resulting, often insoluble precipitates [11]. Another potential molybdenum source is $MoCl_5$ [11], while compounds such as H_2MoO_4 and MoO_3 are less often used due to their low solubility [5].

For the application of such materials in energy storage, the formation of nanoscopic precursors would be very attractive, especially if the precursor can be transformed into

the desired molybdenum carbide without losing the initial morphology. In addition, the large-scale production of such materials is important since relevant amounts have to be produced. In previous studies of our group, it was shown that precipitation methods, which are commonly conducted in batch processes, can be transformed into a continuous process by applying a microjet reactor [23,24]. Consequently, the possibility of a large-scale production of well-defined (nano)particles is opened up. In this procedure, two reactant solutions are fed into a reaction chamber under high pressure, which initiates the nucleation process through rapid mixing. The mixed product is removed from the mixing chamber by a gas jet, and particle growth takes place on the path to the collection container. Isolating nucleation and growth enable a high degree of control over particle properties. We have applied this method already to the formation of silicon oxide carbides species for battery applications [25–27].

Based on the work of Ge et al. [8], where Mo_2C nanoparticles are prepared by direct pyrolysis of their MoO_x/p-phenylenediamine hybrid precursors, we optimize in our previous work the synthesis to transfer this procedure to the microjet reactor [28,29]. This synthesis was further modified by changing the organic component for the presented study.

Herein, we report a systematic study on the formation of precursors and the synthesis of molybdenum carbides, nitrides, oxides, and $Mo(C,N,O)_x$ composite materials. The effects of the precursor ratio and the influence of different organic species were evaluated to further explore the role of carbon sources for pyrolysis. In our work, we mainly focus on the different amines used, the influence of the ratios used, and the resulting compounds, as well as their composition after pyrolysis.

The aim of the study was not to obtain phase-pure materials but to investigate the influence of different diamines on the final composition of the precipitated as well as the pyrolyzed compounds. This work follows on from two of our previously published papers [28,29]. There, the synthesis and pyrolysis of the precursor using para-phenylenediamine (PPD) was investigated. The present study builds on these earlier results. Using different amines, the overall influence of organic species in the synthesis of such molybdenum carbides, nitrides, oxides, and $Mo(C,N,O)_x$ composite materials is compared.

2. Materials and Methods

2.1. Materials

Ammonium heptamolybdate tetrahydrate ($(NH_4)_6Mo_7O_{24}{\cdot}4\ H_2O$, AHM; ≥99%) and hexamethylenediamine (HMD; ≥99.5%) were obtained from Carl Roth GmbH & Co. KG, Karlsruhe, Germany. 1,8-diaminonapthalene (1,8-DAN; 97%) was purchased from Alfa Aesar, Haverhill, MA, USA. Hydrochloric acid (HCl; 37%) was obtained from Bernd Kraft GmbH, Oberhausen, Germany. Ethanol (99% denatured with 1% PE) was received from BCD Chemie GmbH, Hamburg, Germany. All chemicals were used without further purification.

2.2. Syntheses—Microjet Synthesis of Precipitates

Diluted hydrochloric acid (between 0.05 and 0.6 mmol L^{-1}, solution A) and a combination of an aqueous AHM solution and an ethanolic solution of 1,8-DAN or an aqueous solution of HMD (solution B) (Tables 1 and 2) were used in the synthesis. The solutions were pumped into the reactor using two HPLC pumps (LaPrep P110 preparative HPLC pumps (VWR)) at a flow rate of 250 mL min^{-1}. In the microjet reactor, the solutions collide through a nozzle with a diameter of 300 µm and a strong mixing takes place under high pressure. The resulting particle suspensions were removed with a stream of nitrogen gas at a pressure of 8 bar [23]. Each reactant starting solution (solution A and solution B) had a volume of 1 L. Both solution jets collide at an angle of 180° to each other, while the nitrogen stream enters the reaction chamber at an angle of 90° to the nozzles and the outlet pipe is at an angle of 180° to the nitrogen stream A schematic illustration of the experimental setup is shown in Figure 2.

Table 1. The syntheses of the precursors 1,8-DAN/molybdate and the different ratios in the mixing solution.

Reaction Number	Ratio (1,8-DAN:AHM)	1,8-DAN (g) (mmol)	AHM (g) (mmol)	HCl (M)
1	1:1	0.5 3.16	3.86 3.12	0.05
2	2:1	1.0 6.32	3.86 3.12	0.05
3	5:1	1.25 7.90	1.93 1.56	0.025
4	9:1	2.33 15	1.93 1.56	0.025
5	10:1	2.5 16	1.93 1.56	0.025
6	15:1	3.75 24	1.93 1.56	0.05
7	18:1	4.375 28	1.93 1.56	0.05
8	20:1	5.16 33	1.93 1.56	0.05
9	25:1	6.09 38	1.93 1.56	0.075
10	30:1	7.34 46	1.93 1.56	0.1

Table 2. The syntheses of the precursors HMD/molybdate and the different ratios in the mixing solution.

Reaction Number	Ratio (HMD:AHM)	HMD (g) (mmol)	AHM (g) (mmol)	HCl (M)
1	1:1	0.365 3.14	3.86 3.12	0.2
2	2:1	0.725 6.24	3.86 3.12	0.2
3	5:1	1.815 16	3.86 3.12	0.3
4	9:1	3.265 28	3.86 3.12	0.3
5	10:1	3.63 31	3.86 3.12	0.3
6	15:1	5.445 47	3.86 3.12	0.3
7	18:1	6.535 56	3.86 3.12	0.4
8	20:1	7.01 60	3.86 3.12	0.4
9	25:1	9.075 78	3.86 3.12	0.6
10	30:1	10.89 97	3.86 3.12	0.6

Once synthesized in the microjet reactor, the particles were separated by centrifugation (8000 rpm, 15 min). Products were washed with ethanol and dried at 80 °C.

Finally, the precursors obtained were pyrolyzed under argon flow using the following temperature program (Figure 3).

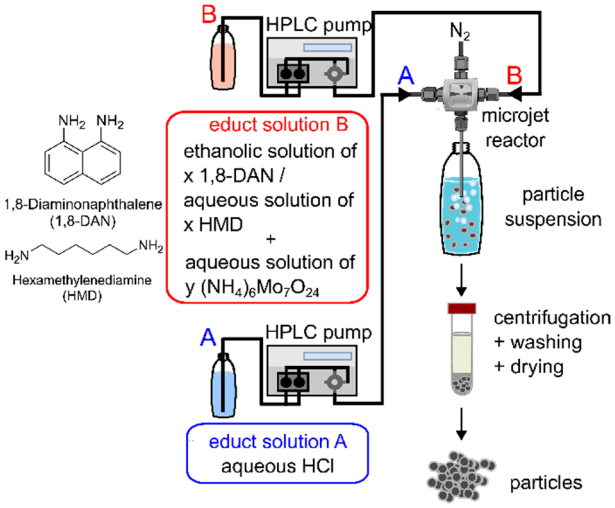

Figure 2. General reaction scheme showing the continuous wet-chemical synthesis of the products 1,8-DAN/molybdate and HMD/molybdate.

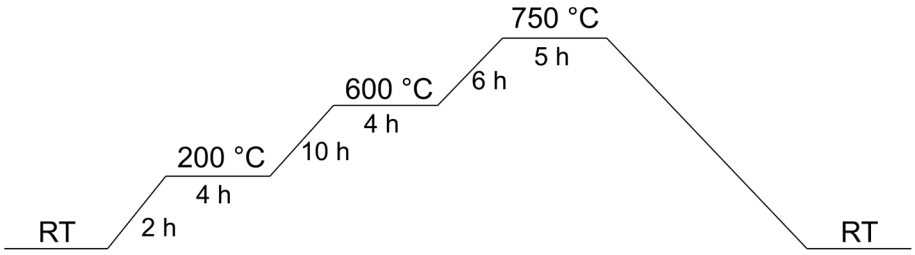

Figure 3. Temperature program for the pyrolysis.

In the 1,8-DAN/molybdate system, the pH values were between 1 and 3. The pH values in the HMD/molybdate system were between 0 and 2.

2.3. Characterization

Fourier-transform infrared spectroscopy measurements (FT-IR) of dried samples were recorded in attenuated total reflectance (ATR) mode using a Bruker Vertex 70 spectrometer (Bruker Optics GmbH & Co. KG, Ettlingen, Germany). Each spectrum was performed in the wave number range of 500–4500 cm^{-1} and by averaging 32 scans with spectral resolution of 4 cm^{-1}. The elemental analyses were conducted on an Elementar Vario Micro cube (Elementar Analysensysteme GmbH, Langenselbold, Germany). Thermogravimetric analyses (TGA) were performed on a Netzsch TG F1 Iris (NETZSCH GmbH & Co. Holding KG, Selb, Germany) under a constant flow of N_2 (40 mL min^{-1}) with a heat rate of 20 K min^{-1} and until 1173 K. During the measurements the samples were placed in an open alumina crucible. Powder X-ray diffraction (XRD) measurements were carried out on a Bruker D8-A25-Advance diffractometer (Bruker AXS GmbH & Co. KG, Karlsruhe, Germany) in a Bragg–Brentano geometry with CuK_α-radiation. The XRD patterns were performed with a total measurement time of 1 h and from 7 to 110° 2θ with a step size of 0.013°. By the Rietveld analysis, the quantitative analyses were carried out, and the sample composition could be determined by this method using TOPAS 5 [30]. The crystallographic data for the Rietveld refinement were obtained from the Crystallographic Open Database (COD) and the Inorganic Crystal Structure Database (ICSD). Following CIFs were used for Rietveld Refinement Mo_2C [17,20], Mo_2N [31], MoO_2 [32], $MoC_{0.67}$ [21], $MoC_{0.5}$ [22] and Mo [18,33]. SEM images were taken using a JEOL JSM-7000 F microscope (JEOL (Germany) GmbH, Freising, Germany) with a working distance of 10 mm and operating at 20 kV. For the sample preparation, a small amount was placed on a specimen stub covered with a carbon adhesive foil, followed by the deposition of a gold layer.

3. Results and Discussion

3.1. Synthesis/Precipitation Reaction

The first precipitation reaction that was carried out in a continuous process was mixing ammonium heptamolybdate (AHM) as a source of molybdenum with para-phenylenediamine (PPD) in acidic conditions [28]. For the presented study, the organic components were changed to study the influence of an aromatic versus a non-aromatic diamine on their capability as precipitation precursors. The studied diamines were chosen based on their high carbon content and good availability. In addition, potential differences in the precursor production and the final product formation depending on the stereochemistry of the diamines and the extent of aromaticity in the organic molecules can be compared. 1,8-Diaminonaphthalene (1,8-DAN) with a higher organic content in comparison to PPD and hexamethylenediamine (HMD) as a non-aromatic diamine were chosen. The precursors were precipitated by mixing the aqueous solution of AHM as a molybdenum source and an ethanolic solution of 1,8-DAN or an aqueous solution of HMD under acidic conditions (Figure 2). The precipitation reactions were carried out in a microjet reactor using different molar ratios between the molybdenum source and the organic compounds. Subsequently, the correlation between the formation of the molybdenum oxide carbides, carbides, oxides, and nitrides and the composition of the precipitated precursor was investigated.

The precipitation reaction was followed by a subsequent pyrolysis reaction to form molybdenum oxide carbide, carbide, oxide, and nitride (Equation (1)). The organic moieties in the species act as carbon sources during the thermal decomposition. In our approach, we exclusively used amines since other groups, such as hydroxyl, carboxyl, or phosphate groups, can introduce other atoms that can disrupt the delicate reduction equilibrium. These can cause either an excess of various molybdenum oxides or impurities such as phosphorus compounds to be obtained. Only the use of amines leads to the desired molybdenum oxide carbide.

(1)

The precipitates were characterized employing Fourier-transform infrared (FT-IR) spectroscopy, elemental analysis, and thermogravimetric analysis (TGA), as well as scanning electron microscopy (SEM) and powder X-ray diffraction (PXRD).

Comparing the FT-IR spectra of all 1,8-DAN/molybdate precipitates with different ratios indicates a great similarity between these (Supporting Information, Figure S1a). In the spectra of the 1,8-DAN, a broad band in the area of 3550–3350 cm^{-1} can be attributed to the stretching vibration of the N–H group [34,35]. In the spectra of AHM at 3600–3200 cm^{-1}, a broad band indicates the presence of water [36]. These bands almost completely disappear in the 1,8-DAN/molybdate precipitates. All spectra show vibrations at 1650–1550 cm^{-1}, which are caused by the N–H deformation vibrations. In addition, C=C stretching vibrations can be detected in the range of 1500–1480 cm^{-1}. Additionally, typically, molybdate bands are present from 935 to 890 cm^{-1} (Figure 4a). These findings indicate that both organic and inorganic components are integrated in the precipitates [9,37–39]. The N–H deformation vibrations are more pronounced at the higher ratios from 10:1, which indicates a higher amine content in these samples. The vibrations of the molybdate units have the same shape both at low ratios of 1:1 and higher ratios of 10:1. This indicates that the same molybdate cluster must be present.

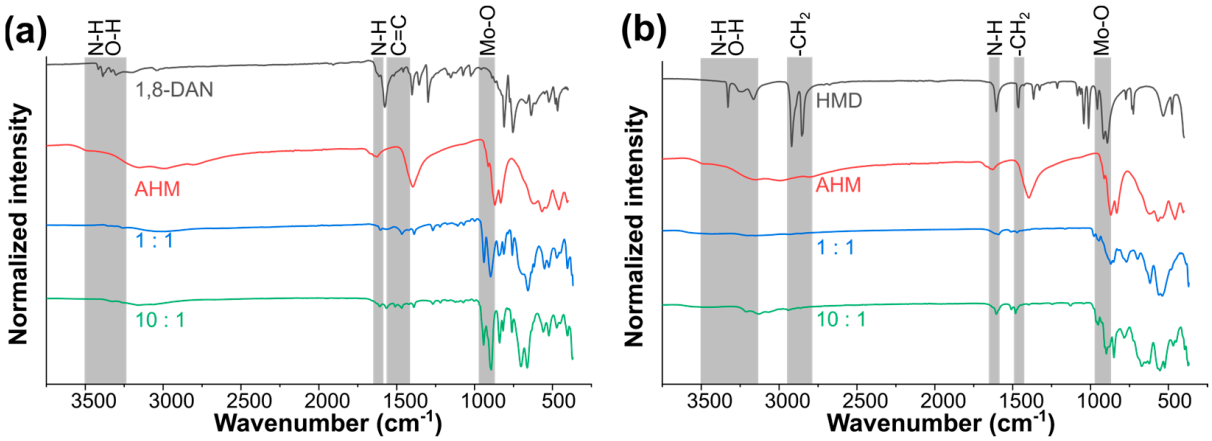

Figure 4. (**a**) IR spectra of the starting materials 1,8-DAN, AHM, and two spectra of a 1:1 and 10:1 mixture. (**b**) IR spectra of HMD/molybdate and their reactants.

In the spectra of HMD, a broad band in the range of 3550–3350 cm^{-1} can be assigned to the stretching vibration of the N–H group [34,40]. Furthermore, two bands appear at 2960–2850 cm^{-1}, belonging to the $–CH_2$ vibrations, while the AHM shows the same vibrations as stated before (vide supra). Again, these bands almost completely disappear in the products of the reaction between HMD and AHM. A comparison of the IR spectra obtained for the different HMD/molybdate ratios revealed two different types of spectra in this system depending on the ratios between the components (Supporting Information, Figure S1b), suggesting the formation of two different compounds. The vibrations at 1650–1550 cm^{-1} of the N–H deformation are visible in all spectra, as well as the $–CH_2$ deformation vibrations, which are detected in the range of 1470–1430 cm^{-1}. Finally, the characteristic bands of the molybdate units are located in the range of 935–890 cm^{-1} (Figure 4b), indicating that both starting materials are found in the precipitate [9,37–39]. There is a more significant N–H deformation oscillation at the higher ratios above 10:1, indicating a higher amine content in these compounds. At the higher ratios, the vibrations of the molybdate units show a shift to higher wavenumbers and a more pronounced peak, indicating a change in the molybdate cluster.

The chemical composition of the precipitates, especially the carbon content, is important for the pyrolytic formation of oxide carbides, carbides, oxides, and nitrides. Therefore, elemental analyses were carried out for all obtained precipitates (Supporting Information, Tables S1 and S2, and Figure S2). Based on these results, two different compositions could be determined. Similar to the results from the IR spectra, the samples with the lower 1,8-DAN content from the ratios 1:1 to 5:1 show similar compositions. This is also the case for the HMD/molybdate precipitates. However, in the latter example, there is no clear trend as the HMD ratio increases. Overall, the amount of carbon increases when more diamine is added to the AHM.

According to the experimental results described until now, the different mixing ratios show different products. Furthermore, different morphologies of the precipitates of 1,8-DAN and molybdate were observed depending on the mixing ratios (Figure 5a and Supporting Information, Figure S3). The first products with the ratio 1:1 and 2:1 show similar block-shaped morphologies. The larger amounts of 1,8-DAN (5:1 to 30:1) lead to highly anisotropic rod-shaped morphologies. Also, in the HMD/molybdate system, different morphologies were observed for the precursor precipitates (Figure 5b and Supporting Information, Figure S4). In this case, the morphologies are more irregularly shaped. The precipitates show agglomerated layered platelets.

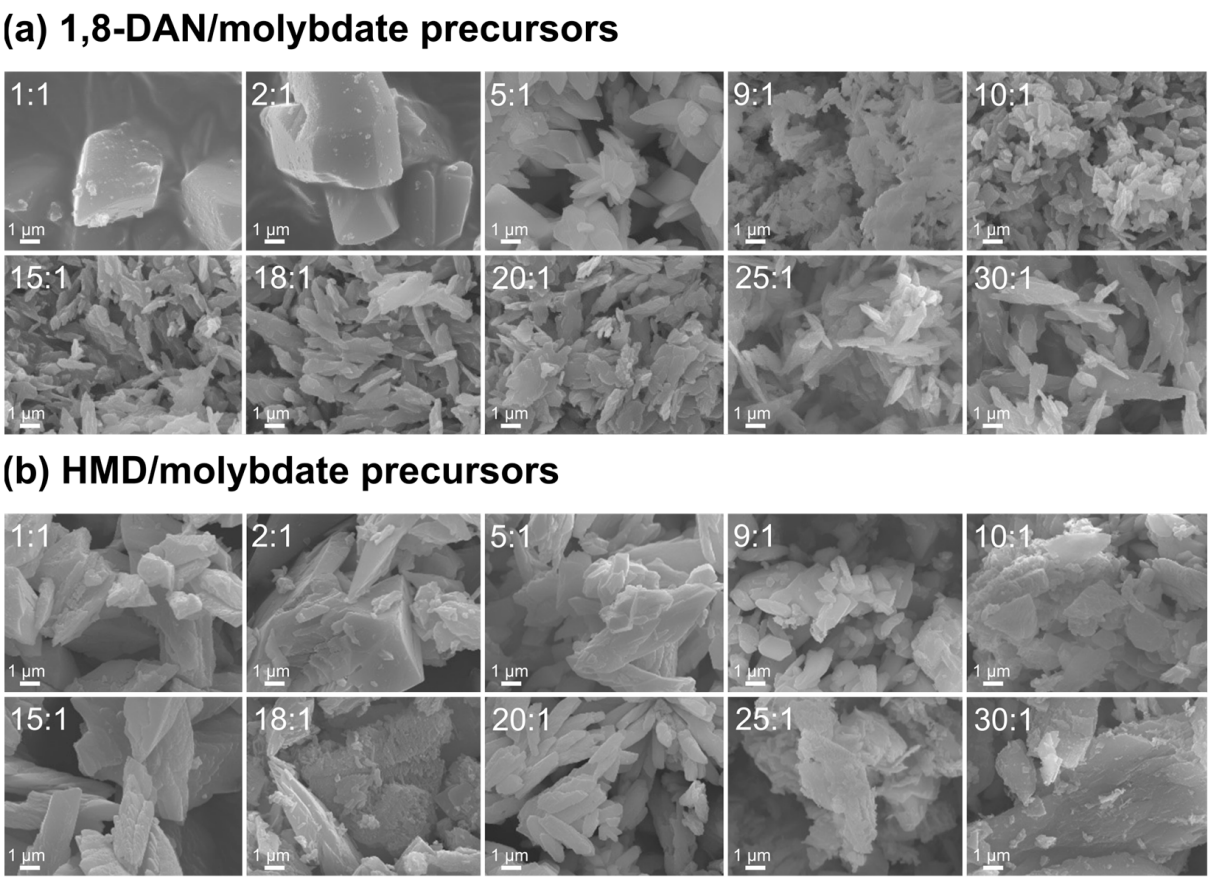

Figure 5. (**a**) SEM images of the products of 1,8-DAN/molybdate precursors with different mixing ratios. (**b**) SEM images of HMD/molybdate precursors.

Both the composition and the synthesis conditions have a strong influence on the morphologies of the precursor systems formed. Since we showed in previous studies that the morphologies of the precipitated products are preserved after pyrolysis, it is therefore possible to adjust the morphology of the pyrolyzed product by adjusting the precursor precipitation reactions. These results are consistent with our earlier findings [28,29].

All precipitates obtained are crystalline phases, as demonstrated by XRD analysis (Figure 6). Based on these measurements, our assumption that different crystalline structures are formed depending on the ratio between the components can be underlined. The diffractograms of the 1,8-DAN/molybdate, again in agreement with the results discussed above, show a transition between a lower ratio of 1,8-DAN (1:1–5:1) and a higher ratio of 1,8-DAN (9:1–30:1) (Figure 6a and Supporting Information, Figure S5a).

The diffractograms of HMD/molybdate do not show such a clear trend, similar to the results of the elemental analysis. The samples with the lower amount of HMD (1:1–5:1) again show the formation of the same compound as the diffraction patterns are similar. Increasing the amount of HMD again leads to similar diffractograms (9:1–30:1) (Supporting Information, Figure S5b). However, closer observation reveals several additional reflections in some diffractograms that could be assigned to the reflections from diffractograms with lower HMD content (1:1–5:1) (Figure 6b). These observed discrepancies most likely also explain the irregular trends in the elemental analysis. It appears that increasing the amount of HMD leads to the mixing of the lower ratio (1:1) and higher ratio (20:1) compounds.

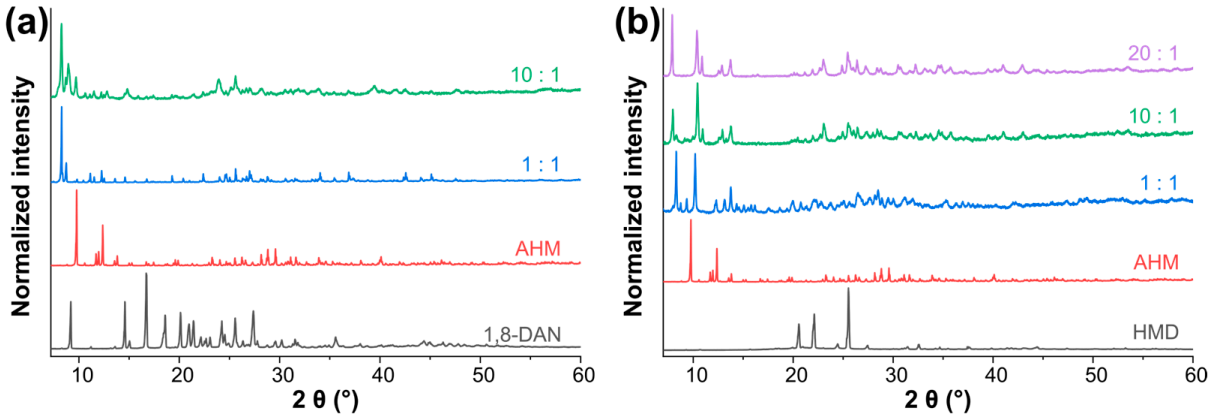

Figure 6. (**a**) XRD pattern of the starting materials 1,8-DAN, AHM, and 1,8-DAN/molybdate (1:1 and 10:1 mixture). (**b**) XRD pattern of the starting materials HMD, AHM, and HMD/molybdate (1:1, 10:1, and 20:1 mixture).

3.2. Thermal Decomposition Behavior of the Precursors

The thermogravimetric analysis (TGA) and TG-FTIR data of the 1,8-DAN/molybdate samples support the hypothesis that two different products were obtained at different ratios (Figures 7a and 8 and Supporting Information, Figure S6). The TGA curves were recorded in nitrogen atmosphere with a heating rate of 20 K min^{-1}. At lower 1,8-DAN to molybdate ratios the release of water, carbon monoxide and carbon dioxide are visible. As the amount of 1,8-DAN increases, the release of ammonia is also observed.

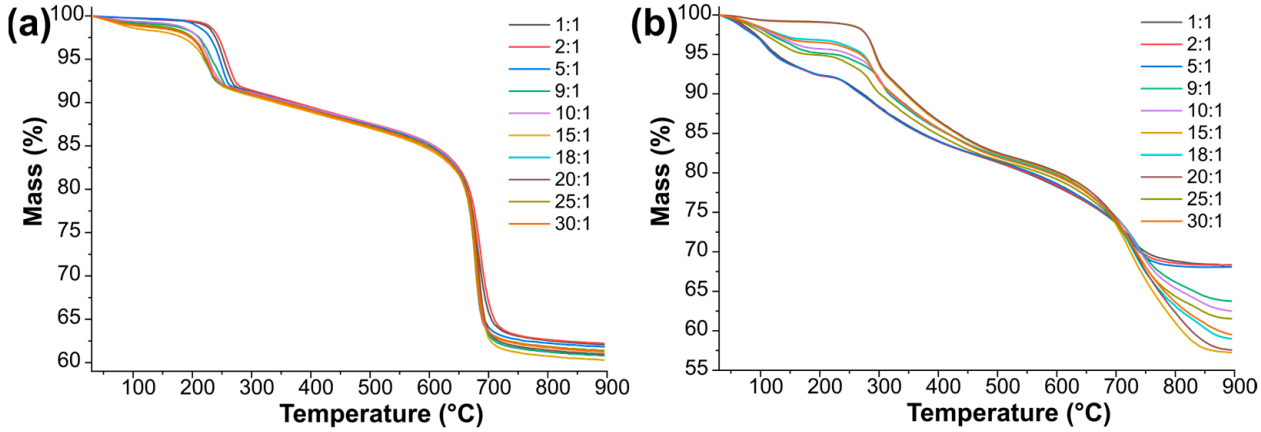

Figure 7. (**a**) Overview of TG curves of 1,8-DAN/molybdate with different ratios; heating rate: 20 K min^{-1}; gas: nitrogen. (**b**) Overview of TG curves of HMD/molybdate with different ratios; heating rate: 20 K min^{-1}; gas: nitrogen.

Furthermore, the TGA and TG-FTIR date of HMD/molybdates samples (Figures 7b and 9 and Supporting Information, Figure S7) also show the formation of two products depending on the respective reactant ratios. At lower HMD ratios, three distinct steps of mass loss are visible, which can be attributed to the loss of water, ammonia, carbon monoxide and carbon dioxide. An increase in the HMD ratio results in the release of less water, more ammonia, carbon monoxide and carbon dioxide.

These results are very similar to the trend of our previous results [28]. In all cases, an increase in the amount of diamine leads to a release of ammonia or an excess of ammonia. The previous results with the PPD/molybdate system show that in the samples with less diamine the diamine is doubly protonated, while in the samples with higher diamine the amine is monoprotonated due to the higher basicity of these samples. The samples with higher diamine also contained ammonium cations (NH_4^+) in order to achieve electroneu-

trality [28]. The release of ammonia observed in the TG-FTIR measurements underlines that the 1,8-DAN/molybdate and HMD/molybdate samples show a similar trend.

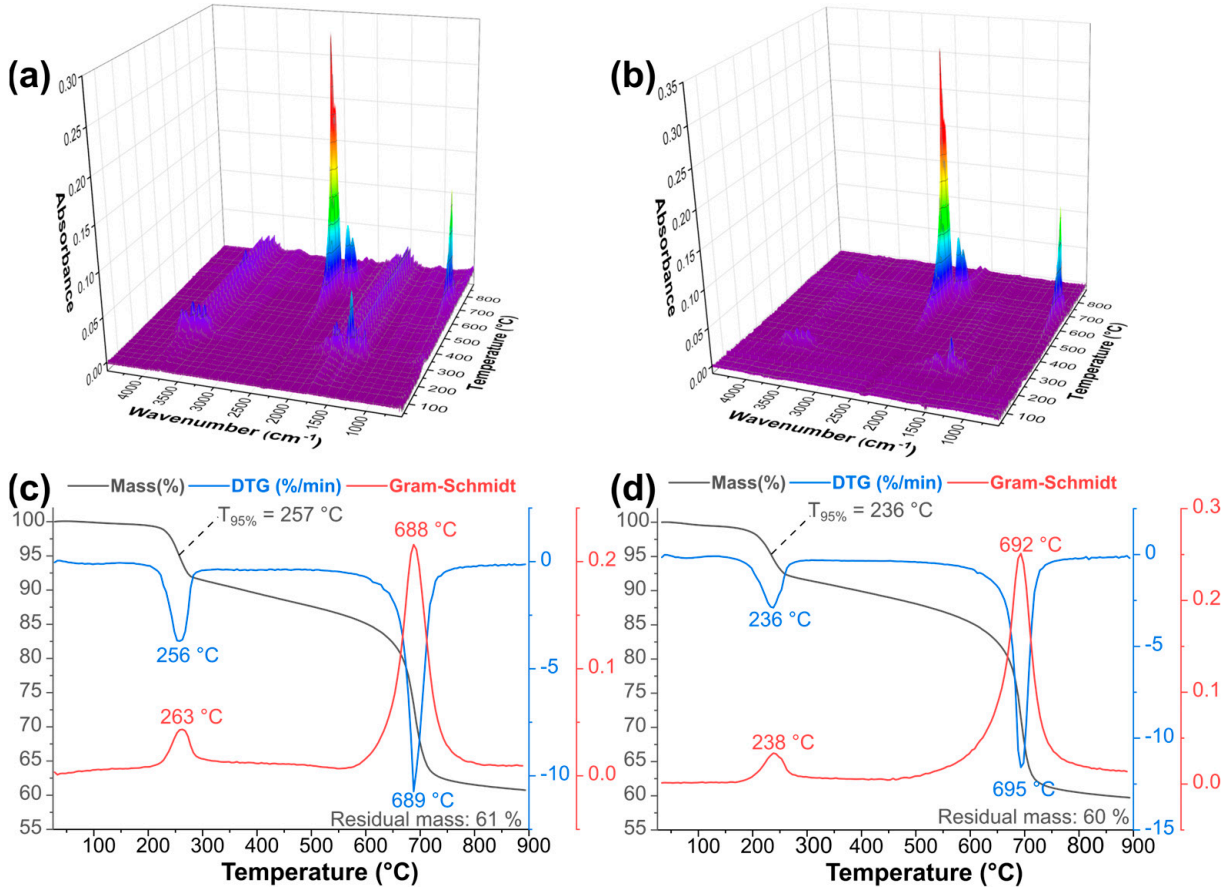

Figure 8. (**a**) TG-FTIR measurements of 1,8-DAN/molybdate (1:1), (**b**) TG-FTIR measurements of 1,8-DAN/molybdate (10:1), (**c**) thermogravimetric curve, with Gram-Schmidt and differential thermogravimetric curve of 1,8-DAN/molybdate (1:1); heating rate: 20 K min^{-1}; gas: nitrogen; (**d**) thermogravimetric curve, with Gram-Schmidt and differential thermogravimetric curve of 1,8-DAN/molybdate (10:1); heating rate: 20 K min^{-1}; gas: nitrogen.

3.3. Pyrolysis of the Precipitation Products

In analogy to our previous work [29], all precursors were heated to 1023 K in an Ar flow and allowed to remain at this temperature for 5 h. As described previously [29], a two-step mechanism takes place during pyrolysis when forming molybdenum carbide from the starting material [6]. Exemplarily, the X-ray diffraction pattern of the decomposed precursor 1,8-DAN/molybdate (1:1) and 1,8-DAN/molybdate (10:1) are presented together with the obtained fit (Figure 10a,b). The presence of orthorhombic Mo_2C [17,20] (*Pbcn*), cubic Mo [18,33] ($Fm\bar{3}m$), and also MoC_x ($Fm\bar{3}m$ or $P6_3/mmc$) [21] was observed. The latter phase is described as a defect structure of the NaCl or NiAs type, whereby not all octahedral voids are filled by carbon atoms. The formation of the respective structure types is attributed to the different carbon content. Because of the uncertainties concerning the elemental composition and thus the amount of x, the composition $MoC_{0.67}$ [21] was used to refine the structure of the NaCl type, while the composition $MoC_{0.5}$ [22] was used for the hexagonal NiAs type.

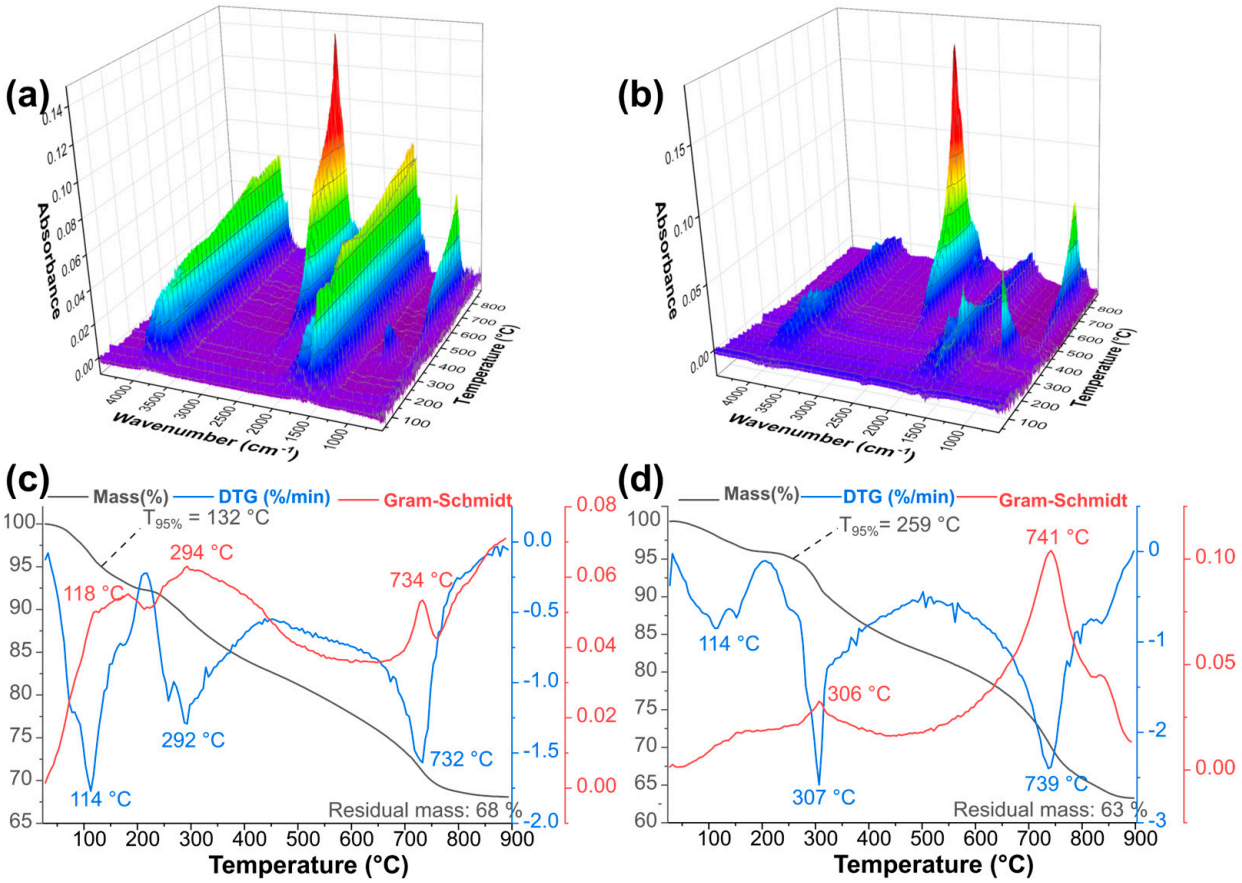

Figure 9. (**a**) TG-FTIR measurements of HMD/molybdate (1:1), (**b**) TG-FTIR measurements of HMD/molybdate (10:1), (**c**) thermogravimetric curve, with Gram-Schmidt and differential thermogravimetric curve of HMD/molybdate (1:1); heating rate: 20 K min^{-1}; gas: nitrogen; (**d**) thermogravimetric curve, with Gram-Schmidt and differential thermogravimetric curve of HMD/molybdate (10:1); heating rate: 20 K min^{-1}, gas: nitrogen.

As described in our previous work [29], stacking faults can be observed in these materials; therefore, the refinement has been conducted using the cubic as well as the hexagonal phase (Figure 10a,b) to model the different stacking periodicities. Metals adapting the Cu-type structure show a similar behavior [41–44]. Representative XRD patterns of the decomposed precursors HMD/molybdate (1:1) and HMD/molybdate (10:1) are shown together with the achieved fit (Figure 10c,d). In contrast to the XRD pattern from the 1,8-DAN/molybdate precursor systems (Figure 10a,b), the XRD pattern from the HMD/molybdate systems (Figure 10c,d) is more crystalline. There is no broad reflection attributable to MoC_x [21], and no amorphous background is visible. The structure refinement revealed the presence of orthorhombic Mo_2C [17,20] besides the presence of monoclinic MoO_2 [32], tetragonal Mo_2N [31], and cubic Mo [18,33].

The pyrolysis of the 1,8-DAN/molybdate precursor was carried out at 1023 K in accordance with our previous experiments [29]. Results from phase composition are presented in Figure 11a. In comparison to the PPD/molybdate system [29], the 1,8-DAN/molybdate precursors mainly form the MoC_x carbide phases besides small amounts of Mo_2C, emphasizing the previous assumption that the pyrolysis process depends on the carbon content in the precursor [29]. This is furthermore in line with the carbon content of PPD (67 mass% C) versus 1,8-DAN (76 mass% C).

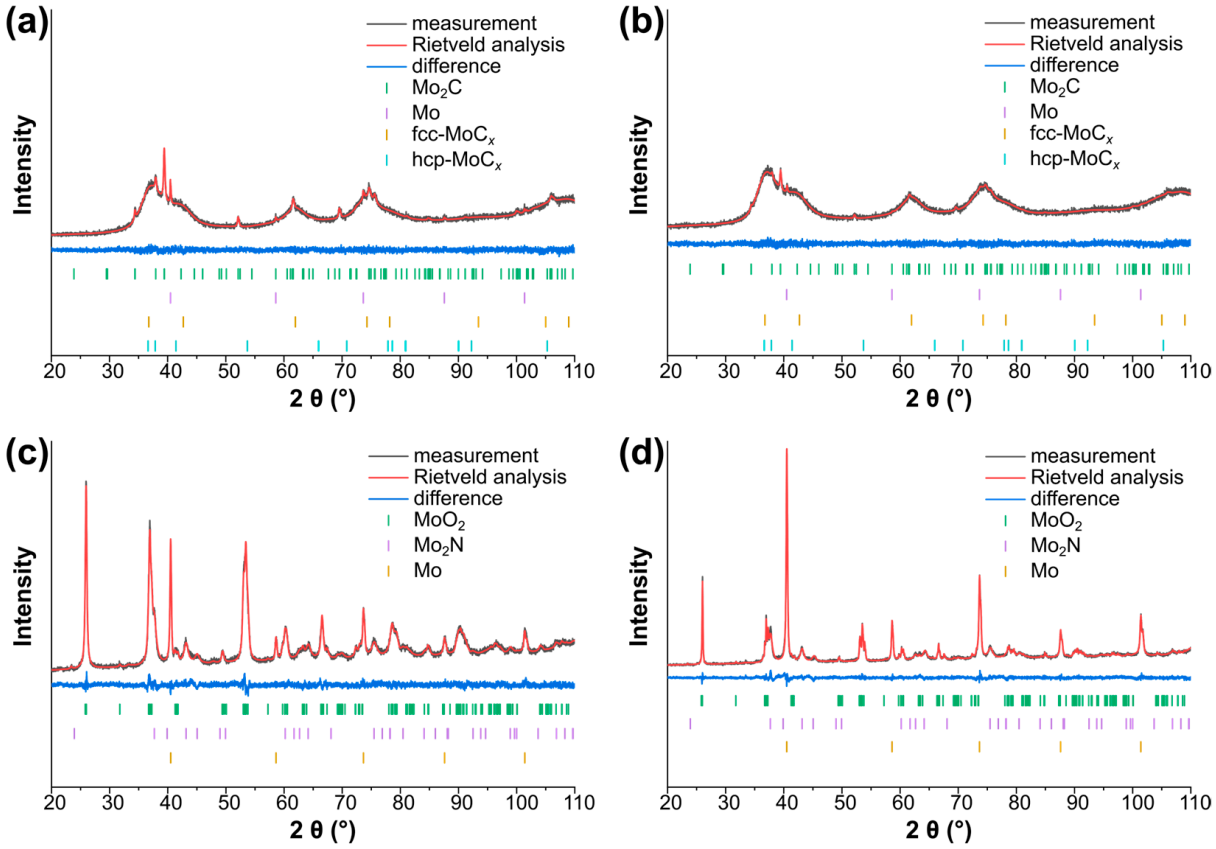

Figure 10. (**a**) Structural analysis of the thermally treated 1,8-DAN/molybdate precursor (1:1) at 1023 K: the refined phase compositions are 78(1) mass% *fcc*-MoC_x, 11(1) mass% *hcp*-MoC_x, 10(1) mass% Mo_2C, and 2(1) mass% Mo. (**b**) Structural analysis of the thermally treated 1,8-DAN/molybdate precursor (10:1) at 1023 K: the refined phase compositions are 87(1) mass% *fcc*-MoC_x, 9(1) mass% *hcp*-MoC_x, 3(1) mass% Mo_2C, and 1(1) mass% Mo. (**c**) Structural analysis of the thermally treated HMD/molybdate precursor (1:1) at 1023 K: the refined phase compositions are 69(1) mass% MoO_2, 21(1) mass% Mo_2N, and 10(1) mass% Mo. (**d**) Structural analysis of the thermally treated HMD/molybdate precursor (10:1) at 1023 K: the refined phase compositions are 39(1) mass% Mo, 33(1) mass% MoO_2, and 27(1) mass% Mo_2N.

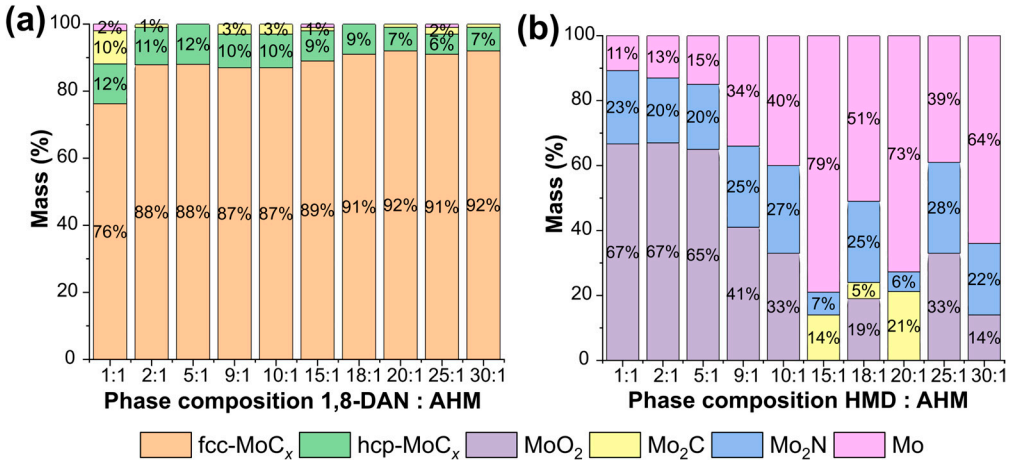

Figure 11. (**a**) Phase compositions of the pyrolyzed 1,8-DAN/molybdate precursors (different phase compositions) determined via fitting the powder X-ray diffraction data. (**b**) Phase compositions of the pyrolyzed HMD/molybdate precursors (different phase compositions) determined via fitting the powder X-ray diffraction data.

HMD/molybdate was pyrolyzed, applying the same parameters as the other two examples. Results from phase composition are presented in Figure 11b. The pyrolysis study of HMD/molybdate with the use of an aliphatic amine does not show a clear trend. In many samples, an increased amount of elemental molybdenum besides MoO_2 is found. Reasons for this divergent trend might be the lower carbon content of HMD (62 mass% C) and its aliphatic nature along with the lower stability (in comparison to aromatic amines) that do not allow for the formation of molybdenum carbide.

The elemental analysis of all pyrolyzed products of 1,8-DAN/molybdate shows a high amount of carbon (Supporting Information, Table S3). This is in contrast to the pyrolyzed samples from the PPD/molybdate system, where only the samples with higher PPD ratios showed higher carbon contents [29]. This is due to the higher carbon content introduced via 1,8-DAN. This excess carbon found in the elemental analysis furthermore indicates that amorphous carbon has to exist in the samples, especially since a high amorphous fraction and no crystalline carbon was observed in the XRD pattern discussed above. Due to an argon atmosphere pyrolysis of the precursors, the resulting particles are embedded in a carbon matrix [1,10,45,46]. Combining molybdenum oxides with carbides and carbonaceous materials creates a potential anode material. For other systems, it has been reported that this can lead to materials that exhibit high capacities along with good cycling stability [1]. The elemental analysis of the pyrolyzed products of the combination between HMD and AHM, again, shows different results. The carbon content in the sample is very low, which is based on the lower carbon content and lower stability of the aliphatic amine (Supporting Information, Table S4). This reveals that the amines decomposed more or less completely via the pyrolysis process.

Finally, SEM images were taken to compare the morphologies before and after pyrolysis. The SEM images before pyrolysis are shown above (Figure 5). In Figure 12a, the corresponding images after pyrolysis of the 1,8-DAN/molybdate precursors are depicted. It is obvious that morphology was preserved after pyrolysis. The SEM images of the HMD/molybdate precursors also indicate the preservation of the morphology after pyrolysis (Figure 12b).

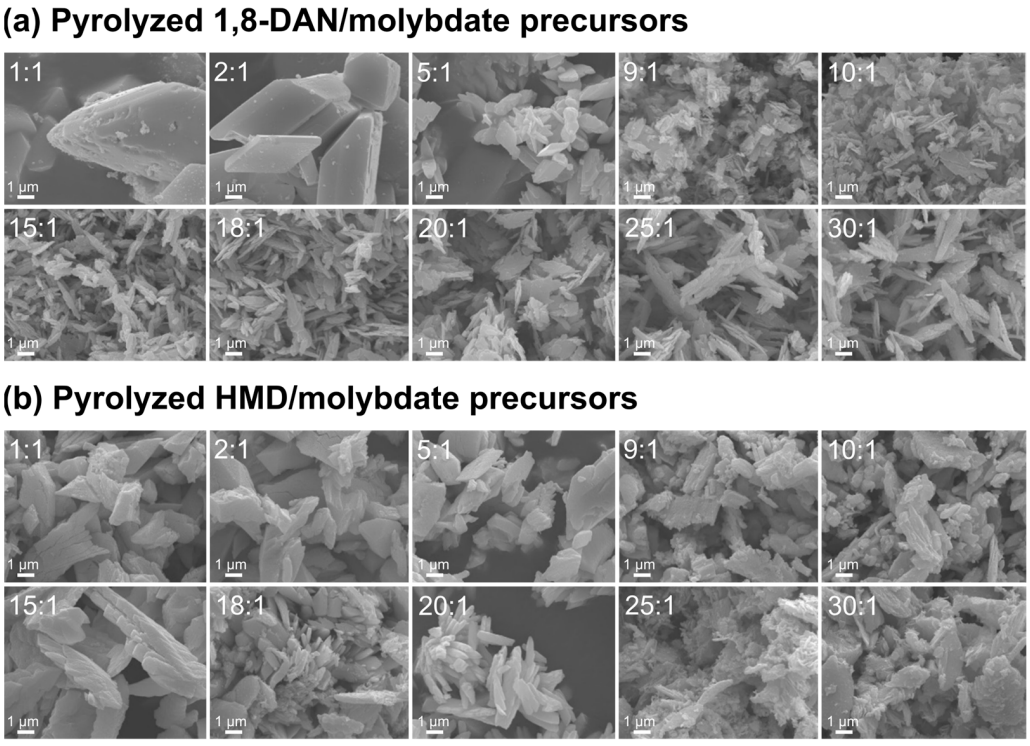

Figure 12. (**a**) SEM images of the pyrolyzed 1,8-DAN/molybdate precursor. (**b**) SEM images of the pyrolyzed HMD/molybdate precursors.

It is interesting to note that there is a great correlation between all reported experiments and our previous results with the PPD/molybdate systems [28,29]. The variation of the ratio between ammonium heptamolybdate and diamine under acidic conditions leads to the formation of two different precipitate compounds with different morphologies. In any case, increasing the diamine amount causes a higher organic content in the precipitate. The results also show the occurrence of ammonium cations with increasing diamine content, which is due to monoprotonated diamines [28]. The pyrolysis of the precursors systems PPD/molybdate [29], 1,8-DAN/molybdate, and HMD/molybdate reveals a similar trend. Pyrolysis of the PPD/molybdate system shows that at low PPD amounts, a mixture of orthorhombic Mo_2C, monoclinic MoO_2, tetragonal Mo_2N, and cubic Mo is formed, while at higher PPD amounts, mainly MoC_x with lower amounts of Mo_2C and elemental Mo is obtained [29]. Similarly to these results, the pyrolysis of the 1,8-DAN/molybdate precursors reveals the formation of MoC_x carbide phases with less impurities of Mo_2C and elemental Mo due to the higher carbon amount in all investigated ratios. Compared to the pyrolysis behavior of PPD/molybdate [29] and 1,8-DAN/molybdate precursors, the HMD/molybdate precursors show a difference. No formation of the MoC_x carbide phases is visible. At lower HMD amounts, mainly MoO_2 was obtained, while at higher HMD amounts, elemental Mo was received. Other side products were Mo_2C and Mo_2N. The low stability of the aliphatic diamine of HMD compared to the aromatic diamine of PPD and 1,8-DAN is the reason for the formation of carbon deficiency in the pyrolysis products of HMD/molybdate precursors. This behavior is also known in the literature. Varganici et al. [47] and García et al. [48] reported higher thermal stability of aromatic compounds compared to aliphatic compounds.

4. Conclusions

The aim of this study was to investigate the synthesis conditions for the preparation of inorganic–organic hybrid materials from ammonium heptamolybdate (AHM) and 1,8-daminonaphthalene (1,8-DAN) or hexamethylenediamine (HMD) utilizing a wet-chemical continuous microjet precipitation method along with subsequent pyrolytic production of molybdenum carbides/nitrides/oxides. For the first step, organic components were selected according to their structure. On the one hand, 1,8-DAN, as an aromatic amine with higher carbon content, was used. On the other hand, hexamethylenediamines, as an aliphatic amine, were utilized. The results clearly show that these differences play a key role in the pyrolysis. Pyrolytic treatment of the 1,8-DAN/molybdate hybrid precursor leads to a variety of composite materials ($Mo(C,N,O)_x$, molybdenum carbide, and molybdenum) embedded in the carbonaceous matrix. The molybdenum carbide MoC_x shows stacking defects, as seen from PXRD measurements. In contrast, the pyrolysis of the HMD/molybdate precursor does not lead to a material with an excess of carbon, which is attributed to the reduced stability and carbon content of the aliphatic amine. It was also shown that the pyrolysis of the inorganic–organic hybrid materials 1,8-DAN/molybdate as well as HMD/molybdate leads to the preservation of the morphology. In the present work, we show that the newly used amines and the newly produced hybrid materials exhibit different behavior in the pyrolysis of the composites than in our previous studies [28,29]. We also observed that different compositions are obtained. Overall, the microjet method enables the synthesis of an extremely interesting hybrid material that could potentially become a candidate as an anode material for Li-ion batteries because of its potentially high capacities and cycling stability over other carbide materials.

Supplementary Materials: The following supporting information can be downloaded at https://www.mdpi.com/article/10.3390/solids5030030/s1, Figure S1: (a) Overview of the received IR spectra of the products from reactions with different ratios of 1,8-DAN/molybdate. (b) Overview of the received IR spectra from HMD/molybdate with different ratio; Figure S2: C, H and N mass percent as a function of the ratio of precursors; Figure S3: SEM images of 1,8-DAN/molybdate precursor; Figure S4: SEM images of HMD/molybdate precursors; Figure S5: (a) Overview of the received XRD pattern of the products from reactions with different ratios of 1,8-DAN/molybdate.

(b) Overview of the received XRD pattern from HMD/molybdate with different ratio; Figure S6: TG-FTIR measurements (a) associated FTIR spectra of 1,8-DAN/molybdate (1:1) and (b) associated FTIR spectra of 1,8-DAN/molybdate (10:1); Figure S7: TG-FTIR measurements (a) associated FTIR spectra of HMD/molybdate (1:1) and (b) associated FTIR spectra of HMD/molybdate (10:1); Table S1: Elemental analysis of the precipitated products 1,8-DAN/molybdate; Table S2: Elemental analysis of the precipitated products HMD/molybdate; Table S3: Elemental analysis of 1,8-DAN/molybdate precursors after the pyrolysis; Table S4: Elemental analysis of HMD/molybdate precursors after the pyrolysis.

Author Contributions: Conceptualization, M.A.M. and G.K.; Funding acquisition, G.K.; Investigation, M.A.M. and S.H.; Methodology, M.A.M., O.J. and S.H.; Project administration, G.K.; Resources, G.K.; Supervision, G.K.; Writing—original draft, M.A.M.; Writing—review and editing, O.J. and G.K. All authors have read and agreed to the published version of the manuscript.

Funding: This research received funding from Saarland University and the German Science Foundation (INST 256/349-1 and INST 256/506-1).

Data Availability Statement: The original contributions presented in the study are included in the article/Supplementary Material. Further inquiries can be directed to the corresponding author/s.

Acknowledgments: Instrumentation and technical assistance for this work were provided by the Service Center X-ray Diffraction. We thank Jörg Schmauch for the support with scanning electron microscopy. Special thanks also to Robert Haberkorn for the helpful discussion and advice regarding the Rietveld refinements.

Conflicts of Interest: The authors declare no conflicts of interest.

References

1. Xiu, Z.; Kim, D.; Alfaruqi, M.H.; Song, J.; Kim, S.; Duong, P.T.; Mathew, V.; Baboo, J.P.; Kim, J. Ultrafine molybdenum oxycarbide nanoparticles embedded in N-doped carbon as a superior anode material for lithium-ion batteries. *J. Alloys Compd.* **2017**, *696*, 143–149. [CrossRef]
2. Lu, L.; Han, X.; Li, J.; Hua, J.; Ouyang, M. A review on the key issues for lithium-ion battery management in electric vehicles. *J. Power Sources* **2013**, *226*, 272–288. [CrossRef]
3. Etacheri, V.; Marom, R.; Elazari, R.; Salitra, G.; Aurbach, D. Challenges in the development of advanced Li-ion batteries: A review. *Energy Environ. Sci.* **2011**, *4*, 3243–3262. [CrossRef]
4. Wu, F.; Maier, J.; Yu, Y. Guidelines and trends for next-generation rechargeable lithium and lithium-ion batteries. *Chem. Soc. Rev.* **2020**, *49*, 1569–1614. [CrossRef]
5. Preiss, H.; Meyer, B.; Olschewski, C. Preparation of molybdenum and tungsten carbides from solution derived precursors. *J. Mater. Sci.* **1998**, *33*, 713–722. [CrossRef]
6. Chen, W.-F.; Wang, C.-H.; Sasaki, K.; Marinkovic, N.; Xu, W.; Muckerman, J.T.; Zhu, Y.; Adzic, R.R. Highly active and durable nanostructured molybdenum carbide electrocatalysts for hydrogen production. *Energy Environ. Sci.* **2013**, *6*, 943–951. [CrossRef]
7. Liao, L.; Wang, S.; Xiao, J.; Bian, X.; Zhang, Y.; Scanlon, M.D.; Hu, X.; Tang, Y.; Liu, B.; Girault, H.H. A nanoporous molybdenum carbide nanowire as an electrocatalyst for hydrogen evolution reaction. *Energy Environ. Sci.* **2014**, *7*, 387–392. [CrossRef]
8. Ge, C.; Jiang, P.; Cui, W.; Pu, Z.; Xing, Z.; Asiri, A.M.; Obaid, A.Y.; Sun, X.; Tian, J. Shape-controllable synthesis of Mo_2C nanostructures as hydrogen evolution reaction electrocatalysts with high activity. *Electrochim. Acta* **2014**, *134*, 182–186. [CrossRef]
9. Pang, M.; Wang, X.; Xia, W.; Muhler, M.; Liang, C. Mo(VI)-Melamine Hybrid As Single-Source Precursor to Pure-Phase β-Mo_2C for the Selective Hydrogenation of Naphthalene to Tetralin. *Ind. Eng. Chem. Res.* **2013**, *52*, 4564–4571. [CrossRef]
10. Liu, Y.; Yu, G.; Li, G.-D.; Sun, Y.; Asefa, T.; Chen, W.; Zou, X. Coupling Mo_2C with Nitrogen-Rich Nanocarbon Leads to Efficient Hydrogen-Evolution Electrocatalytic Sites. *Angew. Chem.* **2015**, *127*, 10902–10907. [CrossRef]
11. Giordano, C.; Erpen, C.; Yao, W.; Antonietti, M. Synthesis of Mo and W Carbide and Nitride Nanoparticles via a Simple "Urea Glass" Route. *Nano Lett.* **2008**, *8*, 4659–4663. [CrossRef]
12. Huang, Y.; Gong, Q.; Song, X.; Feng, K.; Nie, K.; Zhao, F.; Wang, Y.; Zeng, M.; Zhong, J.; Li, Y. Mo_2C Nanoparticles Dispersed on Hierarchical Carbon Microflowers for Efficient Electrocatalytic Hydrogen Evolution. *ACS Nano* **2016**, *10*, 11337–11343. [CrossRef] [PubMed]
13. Li, S.; Cheng, C.; Sagaltchik, A.; Pachfule, P.; Zhao, C.; Thomas, A. Metal-Organic Precursor–Derived Mesoporous Carbon Spheres with Homogeneously Distributed Molybdenum Carbide/Nitride Nanoparticles for Efficient Hydrogen Evolution in Alkaline Media. *Adv. Funct. Mater.* **2019**, *29*, 1807419. [CrossRef]
14. Wang, H.-M.; Wang, X.-H.; Zhang, M.-H.; Du, X.-Y.; Li, W.; Tao, K.-Y. Synthesis of Bulk and Supported Molybdenum Carbide by a Single-Step Thermal Carburization Method. *Chem. Mater.* **2007**, *19*, 1801–1807. [CrossRef]

15. Zoller, M.; Bubnova, R.; Biryukov, Y.; Haussühl, E.; Pöttgen, R.; Janka, O.; Penner, S.; Praty, C.; Fitzek, H.; Winkler, J.; et al. Elucidating the physical properties of the molybdenum oxide Mo_4O_{11} and its tantalum substituted variant $Mo_2Ta_2O_{11}$. *Z. Krist.-Cryst. Mater.* **2020**, *235*, 143–155. [CrossRef]
16. Glemser, O.; Lutz, G. Über Molybdänoxyde. *Z. Anorg. Allg. Chem.* **1950**, *263*, 2–14. [CrossRef]
17. Parthé, E.; Sadogopan, V. The Structure of Dimolybdenum Carbide by Neutron Diffraction Technique. *Acta Crystallogr.* **1963**, *16*, 202–205. [CrossRef]
18. Hull, A.W. The positions of atoms in metals. *Proc. Am. Inst. Electr. Eng.* **1919**, *38*, 1171–1192. [CrossRef]
19. Zhu, H.; Li, Z.; Yang, H.; Luo, L. Carbothermic Reduction of MoO_3 for Direct Alloying Process. *J. Iron Steel Res. Int.* **2013**, *20*, 51–56. [CrossRef]
20. Norlund Christensen, A. A neutron diffraction investigation on a crystal of alpha-Mo_2C. *Acta Chem. Scand. Ser. A* **1977**, *31*, 509–511. [CrossRef]
21. Rudy, E.; Brukl, C.E.; Windisch, S. Constitution of niobium (columbium)-molybdenum-carbon alloys. *Trans. Metall. Soc. AIME* **1967**, *239*, 1796–1808.
22. Kuo, K.; Hägg, G. A New Molybdenum Carbide. *Nature* **1952**, *170*, 245–246. [CrossRef]
23. Odenwald, C.; Kickelbick, G. Additive-free continuous synthesis of silica and ORMOSIL micro- and nanoparticles applying a microjet reactor. *J. Sol-Gel Sci. Technol.* **2019**, *89*, 343–353. [CrossRef]
24. Betke, A.; Kickelbick, G. Bottom-Up, Wet Chemical Technique for the Continuous Synthesis of Inorganic Nanoparticles. *Inorganics* **2014**, *2*, 1–15. [CrossRef]
25. Krüner, B.; Odenwald, C.; Tolosa, A.; Schreiber, A.; Aslan, M.; Kickelbick, G.; Presser, V. Carbide-derived carbon beads with tunable nanopores from continuously produced polysilsesquioxanes for supercapacitor electrodes. *Sustain. Energy Fuels* **2017**, *1*, 1588–1600. [CrossRef]
26. Krüner, B.; Odenwald, C.; Jäckel, N.; Tolosa, A.; Kickelbick, G.; Presser, V. Silicon Oxycarbide Beads from Continuously Produced Polysilsesquioxane as Stable Anode Material for Lithium-Ion Batteries. *ACS Appl. Energy Mater.* **2018**, *1*, 2961–2970. [CrossRef]
27. Krüner, B.; Odenwald, C.; Quade, A.; Kickelbick, G.; Presser, V. Influence of Nitrogen-Doping for Carbide-Derived Carbons on the Supercapacitor Performance in an Organic Electrolyte and an Ionic Liquid. *Batter. Supercaps* **2018**, *1*, 135–148. [CrossRef]
28. Abdirahman Mohamed, M.; Arnold, S.; Janka, O.; Quade, A.; Presser, V.; Kickelbick, G. Self-Activation of Inorganic-Organic Hybrids Derived through Continuous Synthesis of Polyoxomolybdate and para-Phenylenediamine Enables Very High Lithium-Ion Storage Capacity. *ChemSusChem* **2023**, *16*, e202202213. [CrossRef]
29. Abdirahman Mohamed, M.; Arnold, S.; Janka, O.; Quade, A.; Schmauch, J.; Presser, V.; Kickelbick, G. Continuous wet chemical synthesis of $Mo(C,N,O)_x$ as anode materials for Li-ion batteries. *J. Mater. Chem. A* **2023**, *11*, 19936–19954. [CrossRef]
30. *AXS*, Topas 5.1; General Profile and Structure Analysis Software for Powder Diffraction Data; Bruker: Karlsruhe, Germany, 2014.
31. Ettmayer, P. Das System Molybdaen-Stickstoff. *Monatshefte Chem.* **1970**, *101*, 127–140. [CrossRef]
32. Bolzan, A.A.; Kennedy, B.J.; Howard, C.J. Neutron Powder Diffraction Study of Molybdenum and Tungsten Dioxides. *Aust. J. Chem.* **1995**, *48*, 1473–1477. [CrossRef]
33. Häglund, J.; Fernndez Guillermet, A.; Grimvall, G.; Körling, M. Theory of bonding in transition-metal carbides and nitrides. *Phys. Rev. B* **1993**, *48*, 11685–11691. [CrossRef] [PubMed]
34. Cataldo, F. On the Polymerization of *P*-Phenylenediamine. *Eur. Polym. J.* **1996**, *32*, 43–50. [CrossRef]
35. Pałys, B.J.; Skompska, M.; Jackowska, K. Sensitivity of poly 1,8-diaminonaphthalene to heavy metal ions-Electrochemical and vibrational spectra studies. *J. Electroanal. Chem.* **1997**, *433*, 41–48. [CrossRef]
36. Ohno, K.; Okimura, M.; Akai, N.; Katsumoto, Y. The effect of cooperative hydrogen bonding on the OH stretching-band shift for water clusters studied by matrix-isolation infrared spectroscopy and density functional theory. *Phys. Chem. Chem. Phys.* **2005**, *7*, 3005–3014. [CrossRef]
37. Shi, Z.; Gao, B.; Mo, Q.; Shao, Z.J.; Nie, K.; Liu, B.; Zhang, H.; Wang, Y.; Zhang, Y.; Gao, Q.; et al. Organic-Inorganic-Hybrid-Derived Molybdenum Carbide Nanoladders: Impacts of Surface Oxidation for Hydrogen Evolution Reaction. *ChemNanoMat* **2018**, *4*, 194–202. [CrossRef]
38. Gao, Q.; Yang, L.; Lu, X.; Mao, J.; Zhang, Y.; Wu, Y.; Tang, Y. Synthesis, characterization and lithium-storage performance of MoO_2/carbon hybrid nanowires. *J. Mater. Chem.* **2010**, *20*, 2807–2812. [CrossRef]
39. Gao, Q.; Zhang, C.; Xie, S.; Hua, W.; Zhang, Y.; Ren, N.; Xu, H.; Tang, Y. Synthesis of Nanoporous Molybdenum Carbide Nanowires Based on Organic-Inorganic Hybrid Nanocomposites with Sub-Nanometer Periodic Structures. *Chem. Mater.* **2009**, *21*, 5560–5562. [CrossRef]
40. Kasap, E.; Özbay, A.; Özçelik, S. Infrared spectroscopic study of the Hofmann-diam-type clathrates: M(1,6-diaminohexane)$Ni(CN)_4$ C_6H_6 (M = Ni, Co or Cd). *Spectrosc. Lett.* **1997**, *30*, 491–496. [CrossRef]
41. Wolf, U.; Ernst, F.; Muschik, T.; Finnis, M.W.; Fischmeister, H.F. The influence of grain boundary inclination on the structure and energy of σ = 3 grain boundaries in copper. *Philos. Mag. A* **1992**, *66*, 991–1016. [CrossRef]
42. Hofmann, D.; Ernst, F. Quantitative high-resolution transmission electron microscopy of the incoherent Σ3 (211) boundary in Cu. *Ultramicroscopy* **1994**, *53*, 205–221. [CrossRef]
43. Campbell, G.H.; Chan, D.K.; Medlin, D.L.; Angelo, J.E.; Carter, C.B. Dynamic observation of the FCC to 9R shear transformation in a copper Σ = 3 incoherent twin boundary. *Scr. Mater.* **1996**, *35*, 837–842. [CrossRef]

44. Medlin, D.L.; Campbell, G.H.; Carter, C.B. Stacking defects in the 9R phase at an incoherent twin boundary in copper. *Acta Mater.* **1998**, *46*, 5135–5142. [CrossRef]
45. Wang, R.; Yang, J.; Shi, K.; Wang, B.; Wang, L.; Tian, G.; Bateer, B.; Tian, C.; Shen, P.; Fu, H. Single-step pyrolytic preparation of Mo_2C/graphitic carbon nanocomposite as catalyst carrier for the direct liquid-feed fuel cells. *RSC Adv.* **2013**, *3*, 4771–4777. [CrossRef]
46. Chen, Y.-Y.; Zhang, Y.; Jiang, W.-J.; Zhang, X.; Dai, Z.; Wan, L.-J.; Hu, J.-S. Pomegranate-like N,P-Doped Mo_2C@C Nanospheres as Highly Active Electrocatalysts for Alkaline Hydrogen Evolution. *ACS Nano* **2016**, *10*, 8851–8860. [CrossRef]
47. Varganici, C.D.; Rosu, D.; Barbu-Mic, C.; Rosu, L.; Popovici, D.; Hulubei, C.; Simionescu, B.C. On the thermal stability of some aromatic-aliphatic polyimides. *J. Anal. Appl. Pyrolysis* **2015**, *113*, 390–401. [CrossRef]
48. García, J.M.; Álvarez, J.C.; De La Campa, J.G.; De Abajo, J. Thermal Behavior of Aliphatic-Aromatic Poly(ether-amide)s. *J. Appl. Polym. Sci.* **1998**, *67*, 975–981. [CrossRef]